Shear Strength of Soil Berm During Lateral Buckling of Subsea Pipelines

A. Rismanchian, D.J. White, M.F. Randolph and C.M. Martin

A. Rismanchian: Researcher, University of Western Australia, Australia

D.J. White: Professor, University of Western Australia, Australia

M.F. Randolph: Professor, University of Western Australia, Australia

C.M. Marin: Associate Professor, University of Oxford

Abstract

The soil resistance developed during temperature- and pressure-induced large lateral movements of shallowly embedded subsea flowlines is an important input parameter for the structural design process. A major source of uncertainty in calculation of the soil resistance is the undrained shear strength of the soil berm produced as the flowline moves across the seabed, which is affected by the level of remoulding. To investigate the effect of pipeline embedment and displacement amplitude on the shear strength of the berm, a set of centrifuge model tests was conducted on kaolin clay, involving laterally moving pipelines with constant embedments in the range 5% - 35% of the pipe diameter. Back-analysis of the test results, using finite element limit analysis, showed that the shear strength of the soil berm is a function of pipe displacement amplitude, pipe embedment, and soil sensitivity. On the basis of these results, we propose that the overall berm undrained shear strength may be determined as a convolution of the shear strengths of its constituent soil elements. Finally, a formula is presented for calculating the shear strength of soil elements within the soil berm, and this is used to back-analyse the overall soil berm resistance from the model tests.

1. Introduction

High demand for oil and gas has encouraged the industry to start exploiting fields in very deep seas and far from shore. The hydrocarbon products are transported through pipelines installed on the seafloor. Axial expansion arising from high pressure and high temperature is restricted usually by pipe-soil friction and sometimes by the pipe being anchored to the

seafloor at intervals, which may cause generation of large compressive axial loads in the pipe. Depending on the magnitude of the generated axial loads, the geometry of the pipe, and other factors such as the seabed topography and the pipe out-of-straightness, the pipe may buckle laterally and travel a considerable distance across the seafloor (several pipe diameters), leading to relief of the axial loads.

Because subsea pipelines are subject to regular start-ups and shut-downs, lateral buckling is a cyclic process. If the cycles of bending within a buckle lead to rupture of the pipeline from fatigue, significant environmental impact could result, with far greater consequences than the costs of repair. Therefore, a robust understanding of pipe-soil interaction during buckling is required to ensure that any buckles form in a safe manner, so that the associated risks and the costs of field development are acceptable. A safe scheme to accommodate pipeline expansion loads must be designed, including engineered lateral buckles if required.

On initiation of buckling, as the pipe 'breaks out' laterally, it ploughs a layer of soil in front of its motion direction and creates a berm (White and Dingle 2011; Rismanchian et al. 2012). The pipe motion continues until the lateral resistance from the soil berm balances the driving force. During this lateral motion, the lateral resistance increases as the soil berm in front of the pipe grows. With further motion of the pipe, the thickness of the layer being ploughed typically decreases as the pipe tends to rise, while the soil berm continues to grow and soften. This process continues until the increase in resistance from ploughing fresh soil and pushing a growing berm is counteracted by softening of the soil berm, and as a result the soil resistance approaches a 'residual condition' with essentially constant soil resistance. A source of complexity in assessing pipe-soil interaction during lateral buckling arises from the increase in lateral resistance with growth of the soil berm (geometric hardening) while simultaneously the soil within the berm softens as it is remoulded, potentially reducing the lateral resistance.

In current practice the residual soil resistance is either estimated from site-specific physical model tests (e.g. Bruton et al. 2009) or through empirical equations (e.g. Cardoso and Silveira 2010; White and Cheuk 2010; White and Dingle 2011; DNVGL-PR-F114 2017). Alternatively, large-deformation finite element analyses (e.g. Chatterjee et al. 2012) or large-displacement numerical simulations based on sequential limit analysis (Kong et al. 2018) have been used to analyse the pipe-soil interaction behaviour from pipe breakout to residual conditions.

For some projects, site-specific model tests are conducted to study the soil response during lateral movements of a pipe under constant vertical load, in order to improve estimates of the lateral pipe-soil response. These may be conducted at normal gravity, such as in the facility at the Norwegian Geotechnical Institute (Langford et al. 2007), or in a geotechnical centrifuge. The results of such tests are generally applied to the prototype conditions by curve fitting (e.g. Bruton et al. 2009), and there has been limited development of a theoretical model based on characterisation of the underlying physical processes. Uncertainty therefore remains in the final assessments due to inevitable variations between the pipe and soil properties and operational conditions adopted for the physical models, compared with the final design configurations.

Two of the more recent empirical equations in the literature are by White and Cheuk (2010) and White and Dingle (2011), linking the residual lateral soil resistance to the initial pipe embedment. The latter paper also takes the initial over-penetration ratio of the pipe into account, i.e. the ratio of the initial penetration force to the nominal penetration force arising from pipe self-weight only. In addition, White and Dingle (2011) idealised the berm geometry at residual conditions as a rectangular berm. In this method, the actual height of a berm with partially remoulded strength is replaced by a berm of reduced height, but with full (intact) shear strength. White and Dingle (2011) called the sum of the pipe embedment and the reduced berm height the 'effective embedment' and used equations for the lateral bearing capacity of a pipe at the effective embedment to calculate the residual resistance. Rismanchian (2015) showed that if the remoulded strength of the berm can be predicted, semi-empirical methods such as the 'effective embedment' approach are able to predict the horizontal resistance to an acceptable level of accuracy. However, prediction of the pipe trajectory from which the berm size is calculated remains a challenge in this method.

A major uncertainty in assessing soil resistance during lateral buckling of a pipeline is the modelling of softening within the soil berm. In large-deformation finite element simulations of berm formation, softening is typically incorporated by assuming an exponential decay of shear strength with shear strain (Chatterjee et al. 2012; Kong et al. 2018). The purpose of this paper is to develop a fundamental softening rule for the berm shear strength from back-analysis of physical model experiments, supported by finite element limit analysis. The berm shear strength calculated from the proposed method can be used in semi-empirical methods such as 'effective embedment' (White and Dingle 2011). Alternatively, the proposed softening rule can be used as an input to determine soil berm shear strength in analytical

modelling of soil resistance in field conditions, again drawing on results from finite element limit analysis (Rismanchian 2015).

2. Methodology

A laterally buckling pipeline was modelled physically by moving a short section of a partially embedded model pipe across the surface of a soft clay soil sample, replicating plane strain conditions, while measuring horizontal and vertical loads and displacements. The physical experiments were then modelled numerically and analytically to back-calculate the evolving shear strength of the soil berm. Full details of the model tests are provided by Rismanchian (2015), and are summarised briefly below.

2.1 Physical Modelling

2.1.1 Centrifuge Facility

The experiments were performed at a centrifuge acceleration of 25g, using the beam centrifuge at the University of Western Australia (Randolph et al. 1991; De Catania et al. 2010). The soil sample was prepared in a strongbox with internal plan dimensions of 650 mm × 390 mm and depth of 325 mm.

2.1.2 Soil Sample

The soil was prepared from kaolin clay slurry at a moisture content of twice the liquid limit and was then consolidated under a hydraulic press to a stress of 100 kPa. After removing the soil sample from the press and before starting the tests, sufficient time was allowed for the soil sample to swell, attaining pore-water pressure equilibrium while a layer of water was retained on top of the sample to prevent the sample drying out or being subjected to capillary suction.

The strength of the sample was assessed using a miniature T-bar penetrometer (Stewart and Randolph 1994) with a diameter of 3 mm and model scale penetration rate of 1 mm/s. A T-bar factor of $N_{kt} = 10.5$ was used to convert the net bearing pressure measured by the T-bar to undrained shear strength. The resulting shear strength profile is shown in Figure 1.

Following Wroth (1984), the undrained strength, s_u, at a particular depth in an overconsolidated clay sample was estimated as

$$s_u = \beta\sigma'_v OCR^\Lambda = 0.15(\gamma'z) \cdot OCR^{0.75} \qquad (1)$$

where σ'_v is the in situ vertical effective stress; γ' is the effective unit weight of the soil (measured in the range 6 to 6.5 kN/m^3); OCR is the overconsolidation ratio (for oedometric compression); β is the normally-consolidated undrained shear strength ratio; and Λ is a parameter related to the volumetric stiffness in compression and swelling. Here, Λ and β are taken as 0.75 and 0.15, respectively, which match with the range suggested elsewhere in the literature (e.g. Lehane et al. 2009).

It is appreciated that measuring soil shear strength at shallow depths is prone to error. Since the soil sample was produced carefully under controlled laboratory conditions, and its shear strength profile at depths where the full flow mechanism forms around the T-bar matches well with the non-linear shear strength profile in Equation 1, it is expected that the proposed profile also matches the real shear strength at shallow depths. This is supported by the comparison of a shear strength profile corrected for shallow penetration (White et al. 2010) with the non-linear profile proposed in Equation 1 (see Figure 2).

The average soil sensitivity, S_t, which was measured from deep cyclic T-bar tests (0.5 - 1.5 m deep at prototype scale), was equal to 2.8. The measured apparent sensitivity from a shallow (0.1 - 0.2 m) cyclic T-bar test with water entrainment was equal to 5, although the related degradation curve did not reach a steady state condition by the end of the last cycle.

2.1.3 Model Pipe

The model pipe was fixed rigidly to a bi-directional actuator. The applied vertical and horizontal loads were measured by custom-made strain gauged load cells, either based on bending of a thin-walled tube, or shear deformation of an S-shaped beam. These load cells were used to provide feedback for load-controlled operation on one or both of the vertical and horizontal axes, though the tests reported in this paper did not require load control.

The dimensions and details of the model pipe are given in Table 1. The pipe was fitted with five pore-water pressure transducers (PPTs) at the invert and on each side of the pipe (see Figure 3a). Figure 3b shows the test arrangement and the appearance of the soil surface during a typical test.

2.1.4 Test Programme

The experimental programme comprised a series of swipe tests. In a swipe test the pipe embedment is kept constant during lateral displacement-controlled motion of the pipe. According to plasticity theory of foundation behaviour, for small displacements applied sufficiently rapidly that dissipation of excess pore-water pressure is not allowed, the load path in a swipe test will follow the relevant undrained V-H yield envelope, ignoring minor elastic adjustments (Tan 1990; Martin 1994). Figure 4 illustrates schematically the behaviour that is expected to be encountered in a large-displacement swipe test. As depicted in this figure, the load path initially follows the bonded V-H yield envelope. With further displacement, the suction between the trailing side of the pipe and the soil is broken, and the load path is diverted towards an unbonded V-H yield envelope for the same pipe-soil geometry. After pipe breakout, the load path does not trace a single V-H yield envelope any more. Instead, each swipe provides a locus of V-H points, with each point corresponding to purely horizontal movement (the 'parallel point') on the yield envelope for the current geometrical configuration (i.e. the current berm area, as well as pipe embedment) and the current degree of berm softening. This data is used to monitor the berm softening behaviour during a large-displacement swipe test.

Swipe tests were conducted in six areas of the strongbox, in each of which 4 to 7 individual swipes were conducted with incremental scraping thicknesses ranging between 5% and 35% of the pipe diameter, D. Details of these tests are presented in Table 2, with the test name identifying the area and a sequence number indicating each individual swipe movement. In each area the model pipe was first used to scrape a thin layer of soil from the mudline surface to create a flat datum for the tests. This initial 'swipe' is identified by sequence number zero. For each individual swipe the pipe was penetrated vertically to the relevant predetermined embedment before being pushed laterally for a distance of 7D. At the end of each swipe the pipe was lifted from the soil and moved back laterally to the initial penetration location to start the next swipe, such that the soil surface was progressively lowered by consecutive swipes. The vertical distance between the elevation of the pipe invert in a given swipe, compared with that for the previous swipe, was considered as the scraping thickness, ignoring the negligible rebound of the freshly scraped soil behind the pipe. The zone of bearing failure observed from particle image velocimetry (PIV) and close range photogrammetry (Rismanchian et al. 2012) did not extend much lower than the pipe invert. In addition, the normalised horizontal resistances measured in swipes with similar scraping thicknesses but different depths from the original soil surface were comparable, indicating the negligible

effect of the previous swipe tests at shallower depths on remoulding of the soil below the level of the pipe invert.

To eliminate the influence of the dormant soil berms created by previous swipes in each area, the data following a marked increase in horizontal resistance towards the end of a swipe were removed. Moreover, over-topping of the pipe by the active berm was not observed in any of the tests reported here.

2.2 Finite Element Limit Analysis

Numerical simulations of the experiments were performed using OxLim, a finite element based limit analysis program. The program uses plastic limit analysis to calculate lower and upper bound collapse loads (Makrodimopoulos and Martin 2006, 2007, 2008). The gap between the lower and upper bound solutions is reduced using adaptive mesh refinement as described by Martin (2011). The mesh refinement procedure results in a tight bracket of the exact failure load (typically to ±1%) and reveals the regions of the highest shear strain in the soil, which allows visualisation of the failure mechanism.

In back-analysing the experimental swipe tests, a series of pipe and soil geometries (including a simplified berm geometry) were considered and the vertical and horizontal resisting loads resulting from purely horizontal motion of the pipe were calculated using OxLim. Pipe rotation was prevented, consistent with the model test conditions.

The pipe was modelled as a rigid regular polygon with 1° facets and circumcircle diameter D, while the undrained soil was modelled as a rigid-plastic material following the Tresca yield criterion. Considering the asymmetry of the problem, the whole pipe was modelled with the geometrical boundaries of the soil domain extended to three times the pipe diameter in each direction, i.e. a soil block 6D by 3D, to ensure elimination of boundary effects.

2.2.1 Pipe-Soil Interface

The limiting shear stress between pipe and soil, τ, was calculated from

$$\tau = \alpha \cdot s_u \qquad (2)$$

where α is the interface roughness coefficient. Considering the measured surface roughness of the pipe (Table 1), $\alpha = 0.5$ was assumed in this study.

After lateral breakout, the bond between the pipe's rear face and the soil is broken, leaving no tension between pipe and soil. Since the focus of this study is on pipe-soil behaviour during residual conditions after breakout, a tension cutoff was imposed on the pipe-soil interface in all of the OxLim analyses.

2.2.2 Soil Properties

Since the soil in these experiments was overconsolidated and only a thin layer of soil was scraped during each swipe, a profile of uniform shear strength equal to the shear strength at the pipe invert level was assumed.

The normalised soil weight used in the OxLim analyses was $\gamma'D/s_u = 0.64$, which was the average value of this parameter for all of the experimental tests (with s_u the shear strength of the soil at the pipe invert level). Initial sensitivity analyses showed that degradation of the strength of the soil in a berm has a much greater effect on the horizontal resistance than any slight variations of the effective unit weight; therefore, the value of $\gamma'D/s_u$ was assumed to remain constant.

2.2.3 Hardening Rule

Figure 5 illustrates schematically the formation of a soil berm during pipe penetration and the subsequent growth of an active berm in front of a laterally moving pipe. Geometric hardening was assumed in these analyses, i.e. with the resistance increasing according to the berm size. The area of the berm, A_{berm}, was considered to be equal to the area of displaced soil and was calculated from

$$A_{berm} = A_0 + \int dA = A_0 + \int_0^u t \cdot du \qquad (3)$$

in which A_0 is half of the area of the displaced soil during pipe laying, du is the incremental horizontal displacement, and t is the pipe embedment or scraping thickness at each point. Since in a swipe test t is constant, Equation 2 reduces to

$$A_{berm} = A_0 + t \cdot u \qquad (4)$$

where u is the total horizontal displacement of the pipe.

2.2.4 Geometry

In the initial stages of a swipe test, soil scraped by the pipe is pushed up immediately after being scraped (Figure 6a) then rolls back to the soil surface (Figure 6b) as the pipe continues to displace, owing to the curved shape of the pipe. Up to this point the soil in the berm is not remoulded significantly. Figure 6c clearly shows the existence of a hollow section at the centre of the rolled berm, confirming water entrainment in the berm. This phenomenon is more pronounced for large scraping thickness, while for small scraping thickness, the rolling effect is limited to the first 1D of lateral displacement.

Following this observation, the geometry of the soil berm in the swipe tests was simplified into a square as illustrated in Figure 7. Based on this figure, as the size of the berm grows, the berm geometry is assumed to evolve from ABB′ to ACC′ then to AD′E′F′C′. With further growth of the berm, the size of rectangle CD′E′F′ increases and approaches CDEF. The original intact undrained shear strength was assumed for the soil currently being scraped by the pipe (i.e. all soil below the level ABCD), while the evolving shear strength of the berm was the primary focus of this study.

3. Test Results

3.1 Typical Test Results

As an example of the results from a typical test, Figure 8 shows the horizontal and vertical forces measured in the various swipes in SWP04, normalised by the soil shear strength at pipe invert level and plotted against horizontal displacement. In addition, Figure 9 illustrates the measured V-H load paths and supports the discussions about Figure 4. As mentioned earlier, after breakout, the size of the unbonded V-H yield envelope expands, with the load combination always located at the parallel point of the current V-H yield envelope (illustrated schematically in Figure 4). With this knowledge, the remoulded shear strength of the berm at each location along the pipe trajectory can be back-calculated.

Figure 10 illustrates the geometry of a pipe penetrating the soil at the start of some consecutive swipes. The negative horizontal force during initial pipe penetration, visible in Figure 9, reflects the asymmetry of the soil surface profile created by the previous swipes, as depicted in Figure 10. The slight reduction in vertical force during the time between the end of vertical penetration and the start of lateral pipe movement is a result of stress relaxation attributable to consolidation and creep effects.

3.2 Repeatability of Tests

To show repeatability of the tests, results from all swipes with a scraping thickness of 0.25D are plotted with thin black lines in Figure 11, again normalised by the soil shear strength at pipe invert level. In each graph the thick black line connects the average of the measured values over the range u/D = ±0.05 from selected points with horizontal displacement intervals of 0.5D. This average is used to compare with the analytical results.

There is good agreement between the normalised forces obtained from swipes with similar scraping thicknesses at various soil depths. This indicates the acceptable quality of the fitted shear strength profile, the integrity of the T-bar results, and the repeatability of the test procedure.

4. Analysis of Tests

The method for deriving a fundamental softening rule for berm undrained shear strength is described in this section. It involves the following steps and assumptions:

- First, the shear strength of the berm along the pipe trajectory was back-calculated for each individual swipe using the geometry illustrated in Figure 7.
- Second, the shear strength of the berm from all swipes was described as a function of pipe trajectory (i.e. scraping thickness and horizontal displacement).
- Third, it was assumed that each element of soil in the berm softens independently, and that the mobilised strength of the berm is the volume-averaged strength of its constituent soil elements.
- Finally, softening of each soil element in the berm was defined as a function of the pipe trajectory, intact soil shear strength and soil sensitivity, such that the overall lateral soil resistance was correctly predicted.

4.1 Berm Shear Strength for Each Swipe

The refined mesh zones in Figure 12 represent areas of failure within the soil, obtained from OxLim simulations using the simplified berm geometry described above. A bearing failure mechanism can be identified in front of the pipe and below the original mudline. As a result, the soil elements in this zone will be remoulded with lateral displacement of the pipe,

reducing in strength. However, to simplify the analysis, only softening of soil in the berm (above the original mudline) is considered in this back-calculation of the berm shear strength. This will tend to under-estimate the berm shear strength, to compensate for ignoring any remoulding and softening of soil below the mudline.

Comparing the different subplots of Figures 12 indicates the tendency for the berm strength to affect the failure mechanism. For cases with $s_{u,berm}/s_u = 1$, the failure mechanism is generally a fan zone of distributed shear immediately in front of the pipe, accompanied by a straight failure plane that intersects the ground surface at the front of the berm, regardless of the berm size. For cases with $s_{u,berm}/s_u.=0.25$, the zone of distributed shear sometimes extends through a larger angle, allowing the shear plane to intersect the base of the soil berm and enter the softened soil. In some cases there is a further shear plane at the base of the soil berm (e.g. Fig. 12c) or there is shearing within the berm (e.g. Fig. 12g).

Overall, these variations in the failure mechanism show that softening of the soil within the berm can affect the lateral resistance through a modification of the failure mechanism to pass through the berm. In such cases, the soil elements close to the base of the berm will be more heavily remoulded than the soil at the top of the berm. However, over large distances of pipe movement, which are not captured by the analyses shown in Fig. 12, rotation of the overall berm may tend to distribute the remoulding throughout the berm material, as described in previous observations from experiments using particle image velocimetry (PIV) and close range photogrammetry (Rismanchian et al. 2012).

For each scraping thickness considered, the berm strength was varied between 25% and 100% of the shear strength of the intact soil, and the horizontal and vertical forces were calculated for berms having areas A_{berm} created by horizontal pipe displacements in the range $u/D = 0$ to 5 (see Equation 3). Some typical results of these analyses, for $t/D = 0.25$, are shown as thick coloured lines in Figure 11. Using horizontal displacement intervals of 0.5D, the berm shear strength at each location was calculated from interpolation or extrapolation of the calculated horizontal forces for different berm strengths with respect to the average of the measured forces at the same location. Figure 13 illustrates, for $t/D = 0.25$, the berm shear strength interpolated or extrapolated at different horizontal locations to match the experimental data. All the other scraping thicknesses have a similar trend to this figure. It may be noted from Figure 11 that it was generally not possible to match both the horizontal

and vertical forces between analysis and test data, so attention was focused on the horizontal forces.

For small horizontal displacements, the ratio of the back-calculated berm shear strength to intact soil shear strength in Figure 13 exceeds unity, although this issue was not noticed for swipes with scraping thicknesses lower than 0.1D. Briefly, reasons for this could include:

- The spatial variability of the soil (e.g. the calculated horizontal resistance for $s_{u,berm}/s_u$ = 1.0 at $u/D = 1$ is higher than or very close to the measured value in some tests, but not others).
- The low u/D values coincide with pipe breakout prior to the loss of suction behind the pipe, which would mobilise additional resistance from soil at the rear of the pipe.
- The inherent difficulty of measuring soil shear strength at shallow depths (this may result in lower s_u values than reality, hence producing higher back-calculated berm shear strengths).
- The simplified geometry of berm used in the OxLim analyses.

4.2 Berm Shear Strength in All Swipes

The idealised cumulative shear strains for geometrically similar berms are illustrated schematically in Figure 14, which shows two berms created by a moving blade for two different combinations of scraping thickness and horizontal displacement. Although the berms have different sizes, they are geometrically similar, i.e. $u_1/t_1 = u_2/t_2$. Therefore, the two berms have experienced a similar average shear strain $\overline{\gamma}$. This results in the same amount of remoulding in both berms, which means they will eventually have similar shear strengths. The same argument may be made for the case of the berms created by a laterally moving pipe. As a result, variations of berm strength should be comparable only when the scraped soil has experienced a similar ratio of u/t. Consequently, it is reasonable to plot the normalised berm strength against u/t to assess berm softening. This idea is supported by considering two different plots of the normalised back-calculated berm strength, $s_{u,berm}/s_u$, from all of the experimental swipes. Plotting against u/D leads to scattered data with no clear trend (Figure 15a). However, an acceptable trend emerges by plotting this parameter against u/t (Figure 15b).

The points illustrated in Figure 15b reflect the average back-calculated shear strength within the berm, which is the integrated effect of variations in soil strength over all of the soil

elements in the berm. These elements entered the berm at different times and will therefore have experienced different degrees of remoulding (and hence softening).

4.3 Berm Fundamental Softening Rule

The conceptual model for berm remoulding is illustrated schematically in Figure 16a. The rows of this figure show three stages (denoted I, II, III) of the berm formation and remoulding process. The left hand shows several intact soil elements in front of the pipe being scraped and turned into berm material. Elements in the berm are encompassed by a thick dashed line. The colour of an element indicates its shear strength, denoted by $s_{u,elem}$, which varies from black to pale grey as its strength is reduced from intact to fully-remoulded. In the middle column, each single curved line represents the fundamental softening curve of the corresponding element in the left hand column, identified with a number. The fundamental softening curve is assumed to be the same for each soil element, and is a function of the pipe travel distance since the element entered the berm, normalised by the scraping thickness. The ratio of the shear strength of each element to the intact shear strength of the soil is illustrated by a small black circle. For clarity the fundamental softening curves for stage III (middle plot in bottom row) have been replotted in Figure 16b. The curves in the right hand column of Figure 16a illustrate variations of the berm shear strength ($s_{u,berm}/s_u$) for the berm as a whole, with the horizontal displacement of the pipe again normalised by the scraping thickness, as in Figure 15b. The overall berm shear strength at each stage is shown on this curve with a large circle, and is calculated from

$$s_{u,berm}\left(u,t\right)=\frac{1}{A_{berm}}\sum_{i=1}^{n}A_{elem}\cdot s_{u,elem}$$
(5)

where A_{berm} is the total area of the berm, A_{elem} is the area of the ith soil element, and $s_{u,elem}$ is its shear strength. As indicated in the middle column of Figure 16a, the current element shear strength $s_{u,elem}$ is a function of u_{elem}/t, where u_{elem} is the distance travelled by the pipe from the location at which the element in question was scraped into the berm.

For example, when the pipe starts to move, the shear strength of the soil element #1 will be reduced starting from the intact condition, neglecting any soil softening of the initial berm created during pipe penetration. At the same time, soil element #2 is still intact as illustrated in the middle column of Figure 16a at Stage 1. At this stage, the berm shear strength is equal to the shear strength of element #1. As the pipe moves further, element #2 enters the berm

and starts to be remoulded, while element #1 is further remoulded. Throughout this remoulding process the instantaneous shear strength of element #1 is always less than that of element #2. At stage II in Figure 16a, the berm shear strength is the average of the shear strengths of these two elements, considering their equal sizes. At stage III in Figure 16a, element #1 is fully remoulded while elements #2 to #5 are remoulded to different levels. The idea of inhomogeneity of berm shear strength is supported by the large deformation/displacement analyses of White et al. (2011) and Kong et al. (2018). It is evident from Figure 16 that as the pipe moves further, the shear strength of the berm as a whole is reduced and approaches the fully remoulded shear strength of the soil. In summary, this figure illustrates the proposed analytical framework in which the berm shear strength is determined from a convolution of fundamental softening curves for individual soil elements.

Considering this approach, a fundamental softening rule was proposed in an attempt to generate berm shear strength values consistent with the back-calculated experimental values presented in Figure 15b. This fundamental softening rule is given by an exponential decay function, as used previously by Einav and Randolph (2005):

$$\frac{s_{u,elem}}{s_u} = \delta_{elem} + \left(1 - \delta_{elem}\right) \cdot e^{-\frac{3u_{elem}/t}{(u_{elem}/t)_{95}}} \qquad (6)$$

where δ_{elem} is the reciprocal of the soil sensitivity S_t accounting for water entrainment, and is between 0.10 to 0.35 for kaolin clay (Gaudin and White 2009) depending on the level of water entrainment during the remoulding process. A value $\delta_{elem} = 0.10$ has been assumed for the current experiments (Rismanchian, 2015). The parameter $(u_{elem}/t)_{95}$ is the normalised horizontal displacement at which a soil element in the berm has undergone 95% of the reduction in strength between intact and fully remoulded states, and has been taken as 40.

This softening rule is shown on Figure 17, and has been integrated using Equation 5 to also show the corresponding average strength within the berm. Also shown via markers are the back-calculated experimental values of $(s_{u,berm}/s_u)_{exp}$ for all values of scraping thickness. The experimental trends is captured by the analytical model, although some scatter is present.

The main intended application of Equation 6 is prediction of 'light' pipe lateral buckling behaviour in the field, for which the value of u_{elem}/t starts increasing rapidly immediately

after breakout (u increases and t reduces as the pipe rises towards the mudline). Therefore, during calibration of Equation 6, the maximum possible overlap with $(s_{u,elem}/s_u)_{exp}$ was sought for high u_{elem}/t values, when selecting the value $(u_{elem}/t)_{95} = 40$ (see Figure 17).

Figure 17 illustrates that a freshly scraped soil element is quickly softened within a distance of $u_{elem}/t \approx 10$, after which the rate of softening decreases. Considering the sensitivity of the soil sample in cyclic T-bar tests, $s_{u,elem}$ was not expected to be lower than $0.36s_u$ ($S_t = 2.8 =>$ $\delta_{elem} = 0.36$). However, at $u_{elem}/t = 100$ the back-calculated $s_{u,elem}$ value reduces to 10% of the intact soil strength. This value is supported by soil sensitivity measurements by Gaudin and White (2009), and by measured sensitivities greater than 5 in the current experiments, for situations where water becomes entrained within disturbed soil. Water entrainment and the different mechanism of remoulding (see Figure 6) could have contributed to this higher apparent sensitivity for the berm.

5. Conclusions

A study of subsea pipeline-soil interaction was conducted, employing physical model tests on partially embedded pipelines moving laterally with constant vertical embedment on undrained kaolin clay. Finite element limit analysis was used to back-analyse the horizontal and vertical forces generated during the experimental swipe tests, and it was shown that the overall shear strength of the berm degrades as a function of the ratio of horizontal pipe displacement to scraping thickness.

It was hypothesised that each element of soil in the berm has a different shear strength, which degrades exponentially as a function of the ratio of horizontal displacement to scraping thickness for that element. It was then shown that the overall berm shear strength may be considered as the convolution of the shear strengths of its constituent soil elements.

In the analytical model presented in the current study, the parameters δ_{elem} and $(u_{elem}/t)_{95}$ are unique for each soil, and are related to the sensitivity and ductility of the soil, respectively. Although these parameters are tied to soil type, they should be applicable for a range of pipe weights, diameters and movement patterns on a given soil, removing the necessity of performing several tests covering all these scenarios in order to calibrate a lateral pipe-soil interaction model.

The findings of this study are also applicable to ploughing and bulldozing. In principle, it should be possible to apply the fundamental berm and soil element softening rules proposed in this paper to the behaviour of laterally buckling pipelines in field conditions, where the pipe embedment typically varies with horizontal displacement rather than remaining constant (Rismanchian 2015).

Acknowledgements

References

Bruton, D., White, D. J., Langford, T. and Hill, A. J. (2009). Techniques for the assessment of pipe-soil interaction forces for future deepwater developments. Offshore Technology Conference. Texas, USA, n/a: OTC 20096.

Cardoso, C. O. and Silveira, R. M. S. (2010). Pipe-soil interaction behavior for pipelines under large displacements on clay soils - A model for lateral residual friction factor. Offshore Technology Conference, Houston, USA, n/a: OTC 20767.

Chatterjee S, White D.J, Randolph M.F (2012). Numerical simulation of pipe-soil interaction during large lateral movements on clay. Géotechnique, **62**(8): 693-705.

De Catania, S., Breen, J., Gaudin, C. and White, D. J. (2010). Development of a multiple-axis actuator control system. International conference on physical modelling in geotechnics (ICPMG), Zurich, Switzerland, Taylor & Francis group, London, UK, CD: 325-330.

DNVGL-PR-F114 (2017). Pipe-soil interaction for submarine pipelines. Edition May 2017.

Einav, I. and Randolph, M. F. (2005) Combining upper bound and strain path methods for evaluating penetration resistance. International journal for numerical methods in engineering **63**: 1991-2016

Gaudin, C. and White, D. J. (2009). New centrifuge modelling techniques for investigating seabed pipeline behaviour. Proceedings of the 17th International Conference on Soil Mechanics and Geotechnical Engineering (ICSMGE 2009), The Netherlands, CD: 448-451.

Kong, D, Martin, CM and Byrne, B, (2018). Sequential limit analysis of pipe-soil interaction during large-amplitude cyclic lateral displacements. Geotechnique.

Langford, T., Dyvik, R. and Cleave, R. (2007). Offshore pipeline and riser geotechnical model testing: Practice and interpretation. San Diego, California, USA, n/a: OMAE2007-29458

Lehane, B. M., O'Loughlin, C. D., Gaudin, C. and Randolph, M. F. (2009). "Rate effects on penetrometer resistance in kaolin." Geotechnique **59**(1): 41-52.

Makrodimopoulos, A. and Martin, C. M. (2006). "Lower bound limit analysis of cohesive-frictional materials using second-order cone programming." International Journal for Numerical Methods in Engineering **66**(4): 604-634.

Makrodimopoulos, A. and Martin, C. M. (2007). "Upper bound limit analysis using simplex strain elements and second-order cone programming." International Journal for Numerical and Analytical Methods in Geomechanics **31**(6): 835-865.

Makrodimopoulos, A. and Martin, C. M. (2008). "Upper bound limit analysis using discontinuous quadratic displacement fields." Communications in Numerical Methods in Engineering **24**(11): 911-927.

Martin, C. M. (1994). Physical and Numerical Modelling of Offshore Foundations Under Combined Loads. New College. Oxford, UK, Oxford. **PhD**.

Martin, C. M. (2011). "The use of adaptive finite-element limit analysis to reveal slip-line fields." Géotechnique Letters **1**(April-June): 23-29.

Randolph, M. F., Jewell, R. J., Stone, K. J. L. and Brown, T. A. (1991). Establishing a new centrifuge facility. International conference on centrifuge modelling, Centrifuge 91, Boulder, Colorado, USA.

Rismanchian, A. (2015). Pipe-soil interaction during lateral buckling of marine pipelines. Centre for offshore foundation systems, University of Western Australia, Perth, Australia. **PhD**.

Rismanchian, A., White, D.J. & Dingle, H. R. C. (2012). "Failure mechanisms in soft soil berms during lateral buckling of pipelines: A centrifuge modelling study using PIV

analysis." International Conference Offshore Site Investigation and Geotechnics (OSIG), London, UK.

Stewart, D. and Randolph, M. (1994). T-Bar penetration testing in soft clay. Journal of Geotechnical and Geoenvironmental Engineering, **120**(12): 2230-2235.

Tan, F. S. C. (1990). Centrifuge and theoretical modelling of conical footings on sand. PhD thesis, University of Cambridge.

White, D. J. and Dingle, H. R. C. (2011). "The mechanism of steady 'friction' between seabed pipelines and clay soils." Geotechnique **61**(12): 1035-1041.

White, D. J., Chatterjee, S. and Randolph, M. F. (2011). The use of large deformation finite element analysis to investigate pipe-soil interaction during lateral buckling. SUT Symposium on global pipeline buckling. Perth, Australia, CD.

White, D. J. and Cheuk, C. Y. (2010). SAFEBUCK joint industry project pipe-soil interaction models for lateral buckling design phase II A data review. University of Western Australia and Hong Kong University.

White, D. J., Gaudin, C., Boylan, N. and Zhou, H. (2010). "Interpretation of T-bar penetrometer tests at shallow embedment and in very soft soils." Cnadian Geotechnical Journal **47**(2): 218-229.

Wroth, C. P. (1984). "The interpretation of in situ soil tests." Geotechnique **34**(4): 449-489.

Tables

Figures

Table 1. Model pipe properties

Property	Value
Pipe diameter	20 mm (model scale), 0.5 m (prototype scale, N = 25)
Pipe length	120 mm (model scale)
Pipe surface finish	'Smooth' – finely sandblasted
Pipe surface roughness*	0.5 – 1 µm
Pipe Instrumentation	Five pore-water pressure transducers (PPTs): 1 at the pipe invert, 2 at 45° from the invert (on each side) and 2 at 90° from the invert (on each side)

* Centreline average value, R_a, measured by a profilometer

Table 2. Details of the swipe tests

Test name	Swipe No.	Incremental embedment (D)	Embedment relative to datum (D)
SWP01	SWP01-00	0.10	0
	SWP01-01	0.05	0.05
	SWP01-02	0.05	0.1
	SWP01-03	0.10	0.2
	SWP01-04	0.25	0.45
SWP02	SWP02-00	0.10	0
	SWP02-01	0.10	0.1
	SWP02-02	0.10	0.2
	SWP02-03	0.20	0.4
	SWP02-04	0.05	0.45
	SWP02-05	0.15	0.6
SWP03	SWP03-00	0.10	0
	SWP03-01	0.15	0.15
	SWP03-02	0.05	0.2
	SWP03-03	0.20	0.4
	SWP03-04	0.15	0.55
SWP04	SWP04-00	0.10	0
	SWP04-01	0.20	0.2
	SWP04-02	0.25	0.45
	SWP04-03	0.35	0.8
SWP05	SWP05-00	0.10	0
	SWP05-01	0.25	0.25
	SWP05-02	0.05	0.3
	SWP05-03	0.10	0.4
	SWP05-04	0.35	0.75
SWP06	SWP06-00	0.10	0
	SWP06-01	0.05	0.05
	SWP06-02	0.03	0.08
	SWP06-03	0.07	0.15
	SWP06-04	0.35	0.5
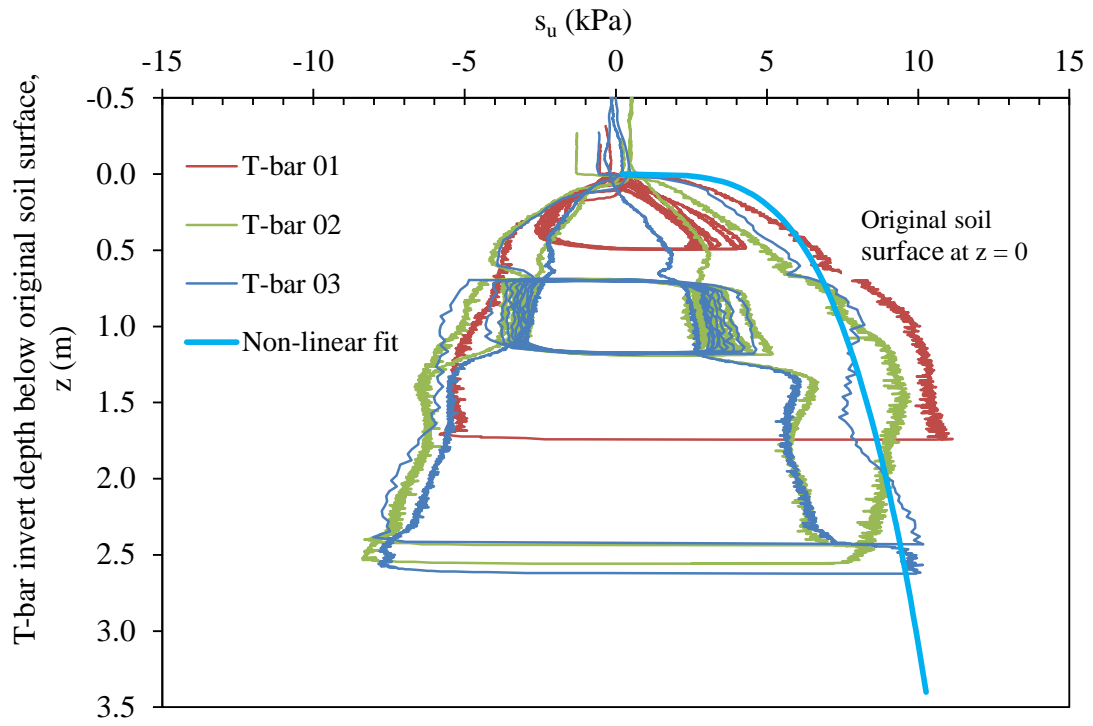
Figure 1. Shear strength profiles measured from T-bar Tests and the adopted shear strength profile.
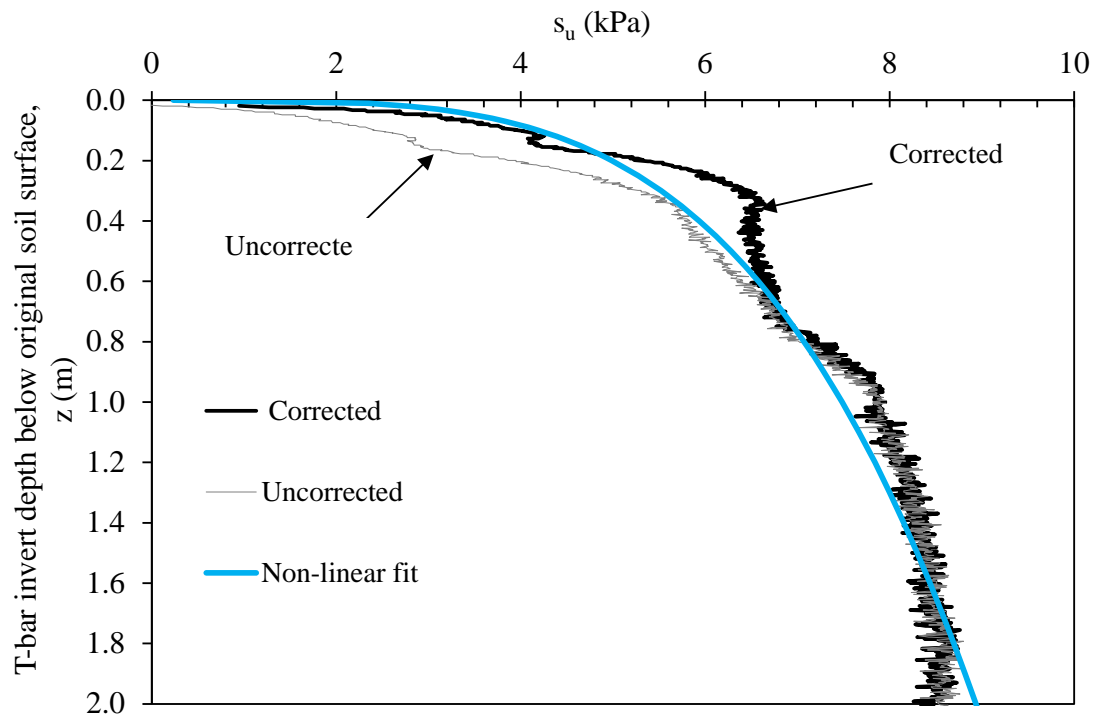
Figure 2. Shear strength corrected for shallow penetration
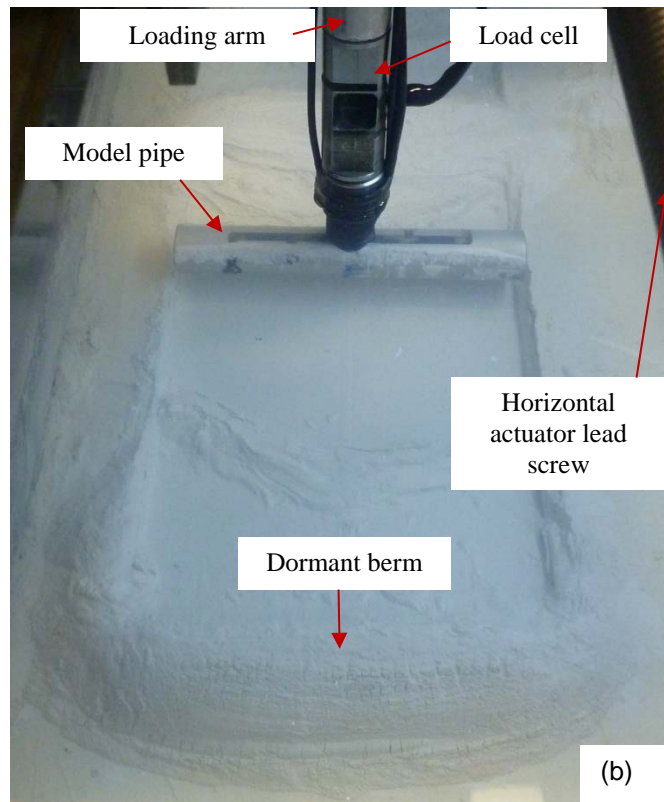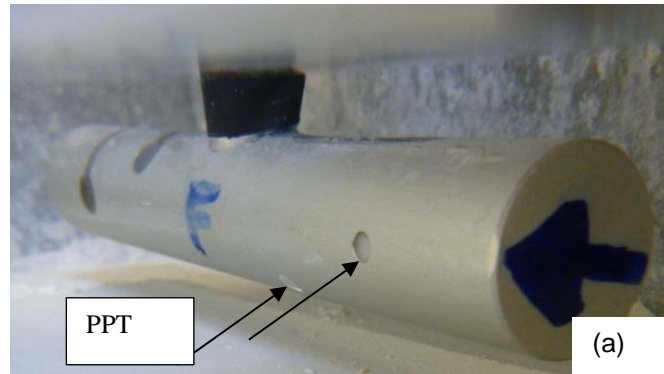
Figure 3. Test arrangement showing (a) PPT arrangements on one side of the model pipe; (b) Appearance of the berms during a test
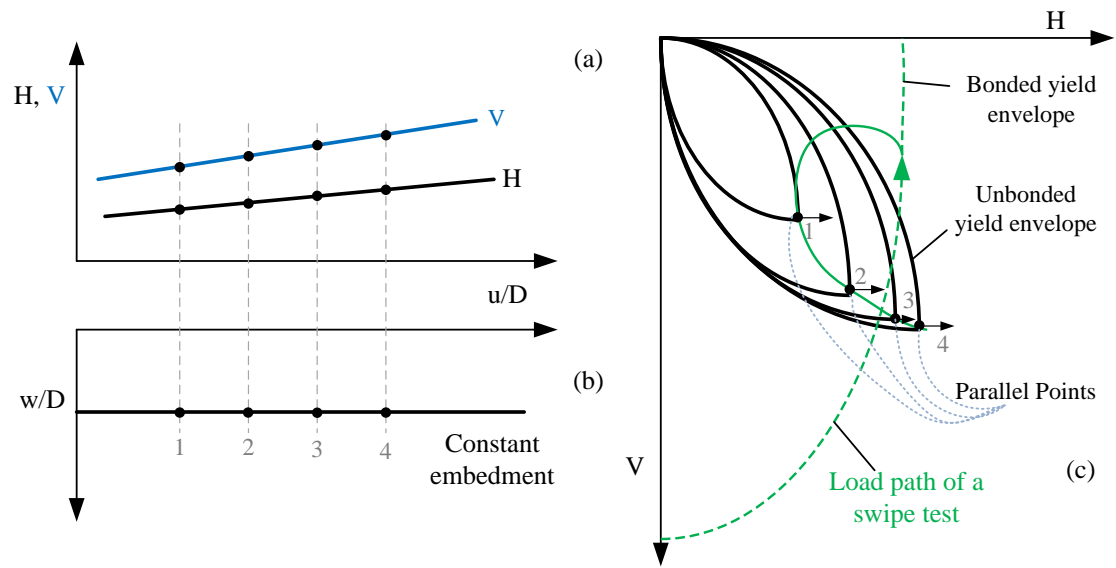
Figure 4. Schematic diagrams of (a) forces, (b) pipe trajectory, and (c) load path during a swipe test
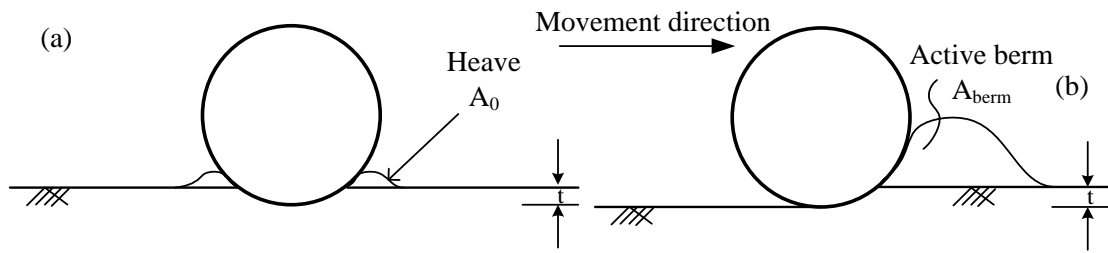
Figure 5. Schematic diagram of (a) pipe penetration; (b) berm growth

Figure 6. Berm formation in a swipe test (a) soil is pushed up shortly after breakout; (b) the berm starts to roll back towards the soil surface; (c) water entrainment within the berm
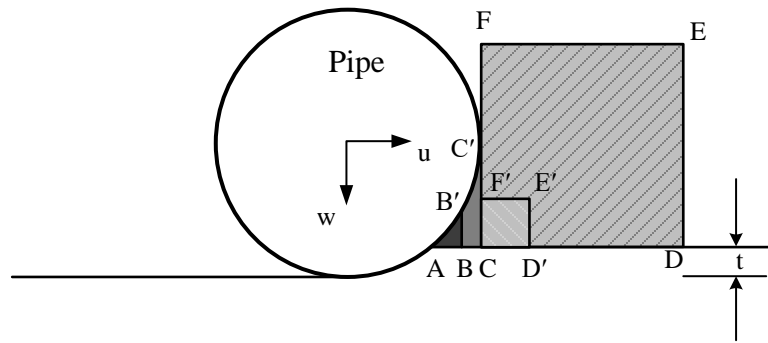
Figure 7. Adopted Geometry for Swipe Tests
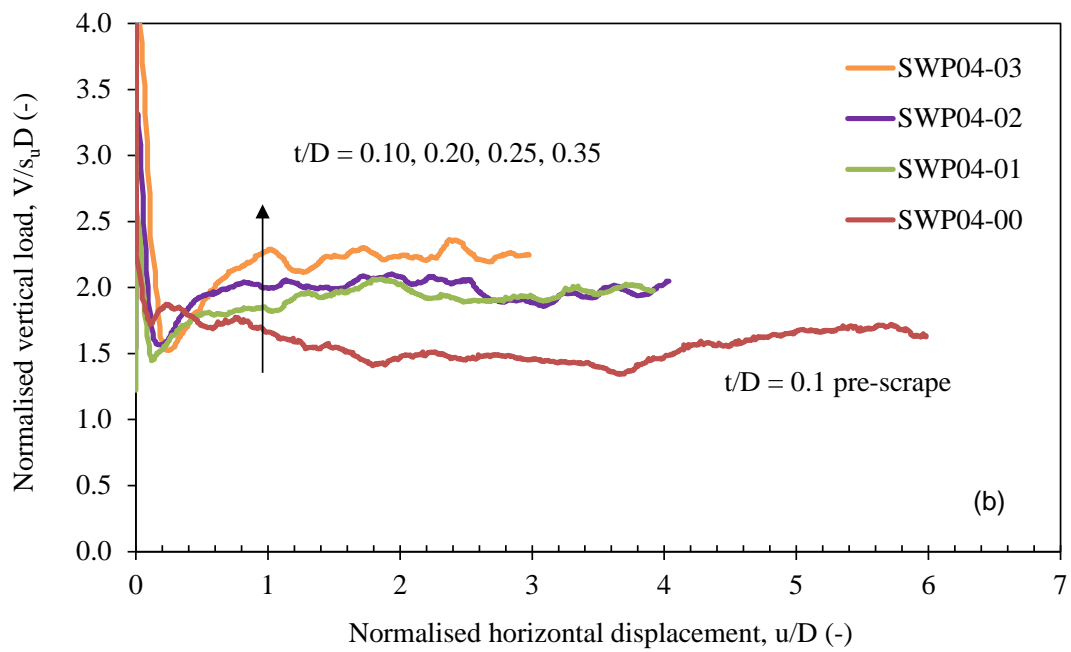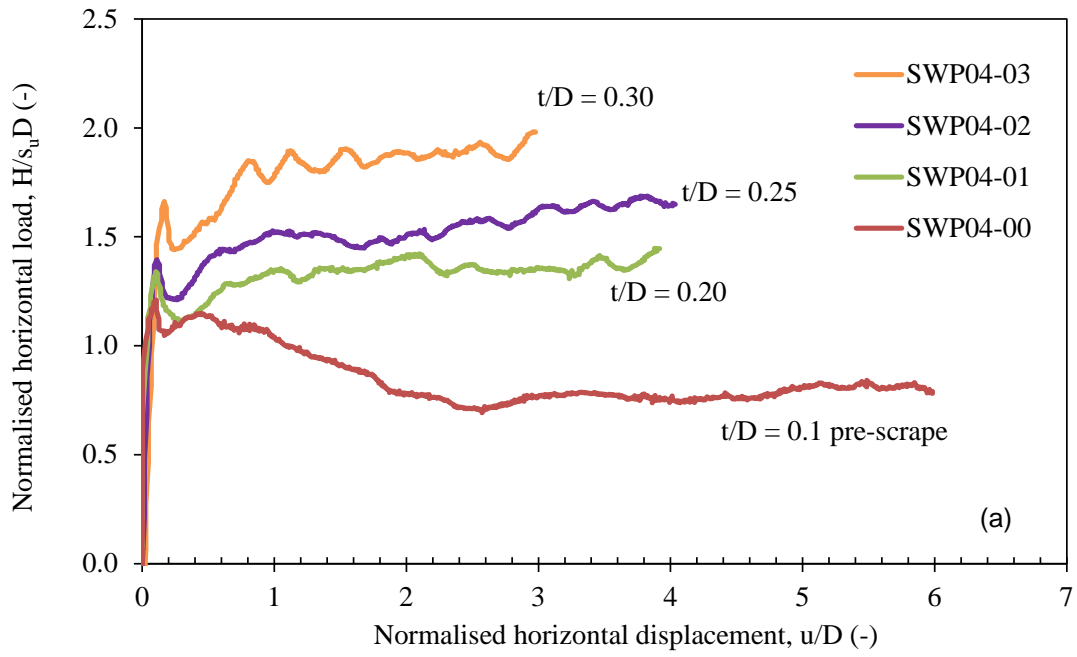
Figure 8. Typical (a) horizontal and (b) vertical forces measured in a swipe test – example from SWP04
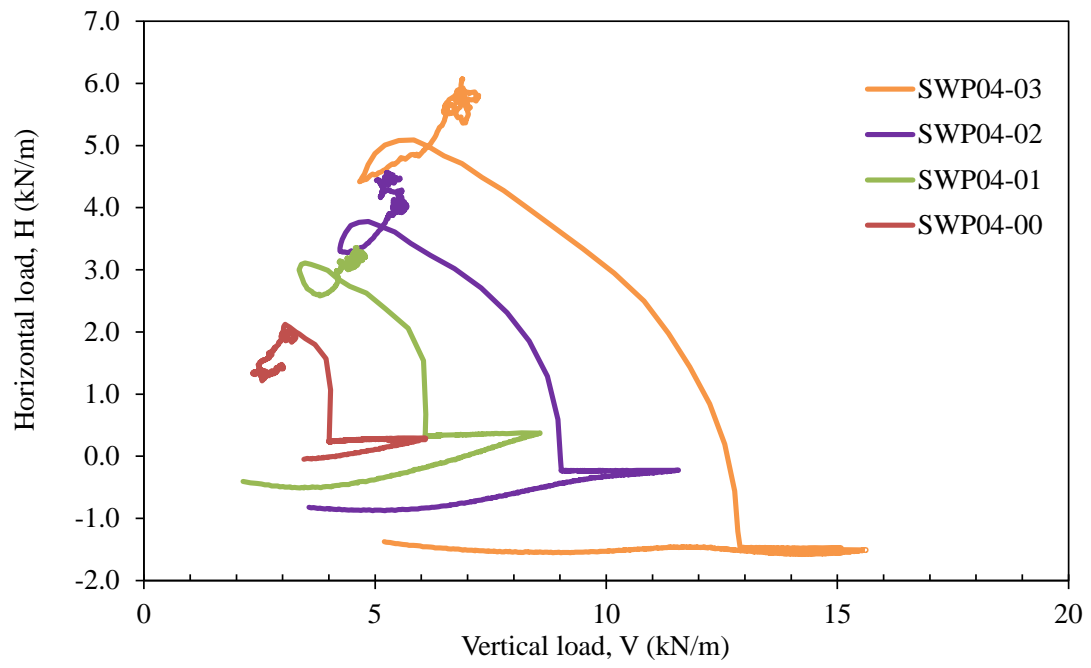
Figure 9. Load path in V-H load space for tests in SWP04 - prototype scale
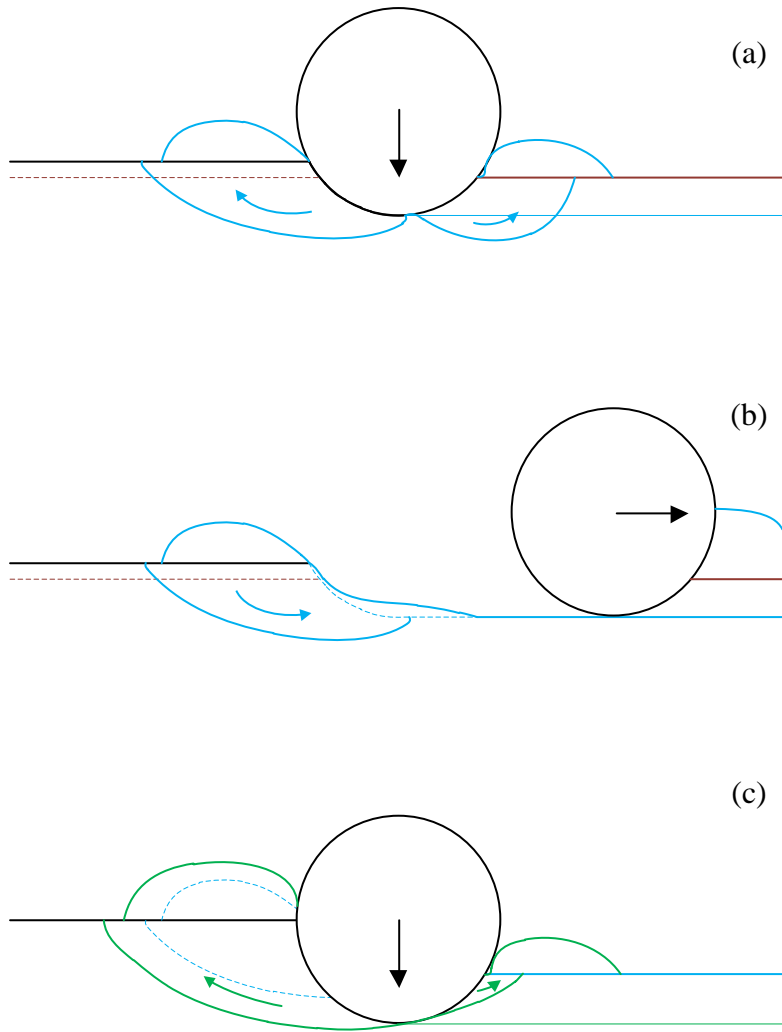
Figure 10. Asymmetric soil geometry at pipe penetration of swipe tests: (a) Pipe penetration; (b) collapse of heaved soil; (c) Failure mechanism during pipe penetration after a few swipes
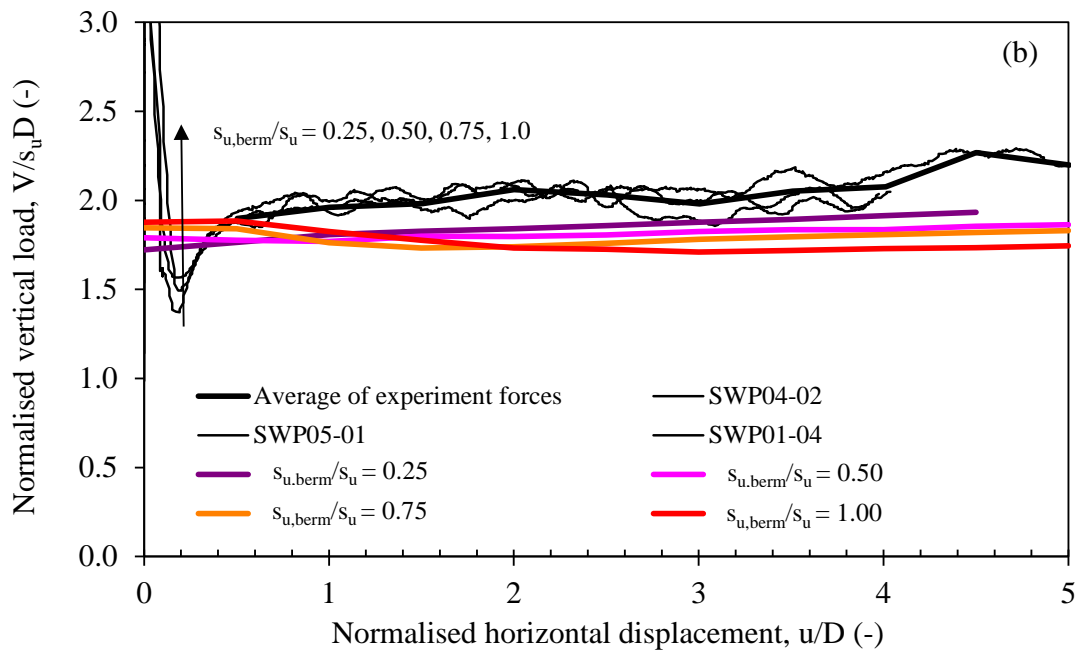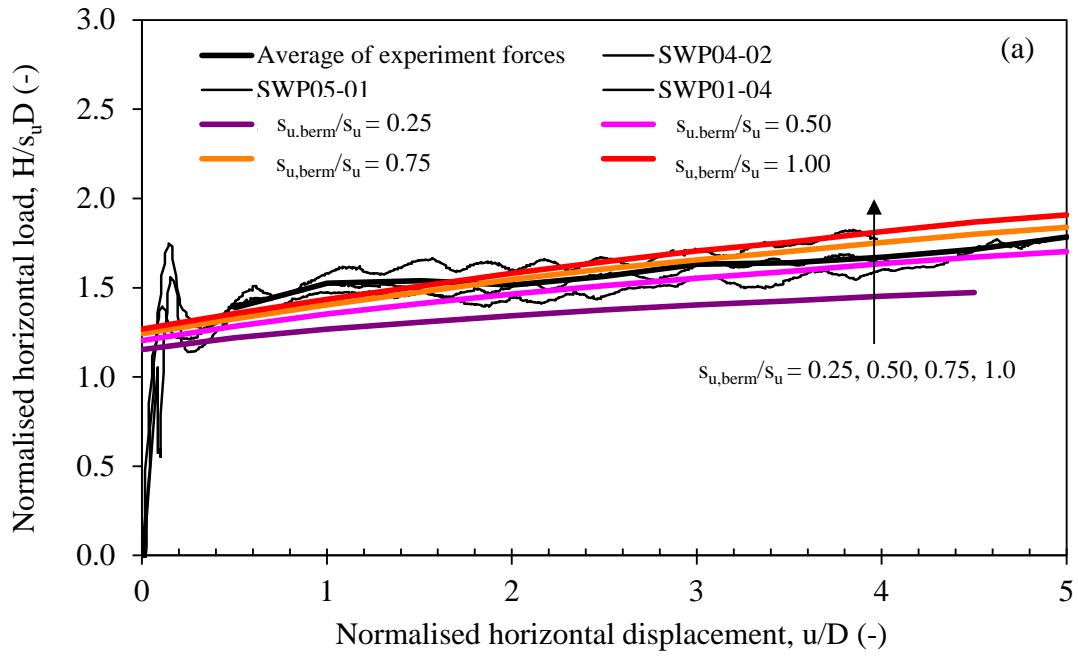
Figure 11. Measured and back-analysed (a) horizontal and (b) vertical forces for t/D = 0.25
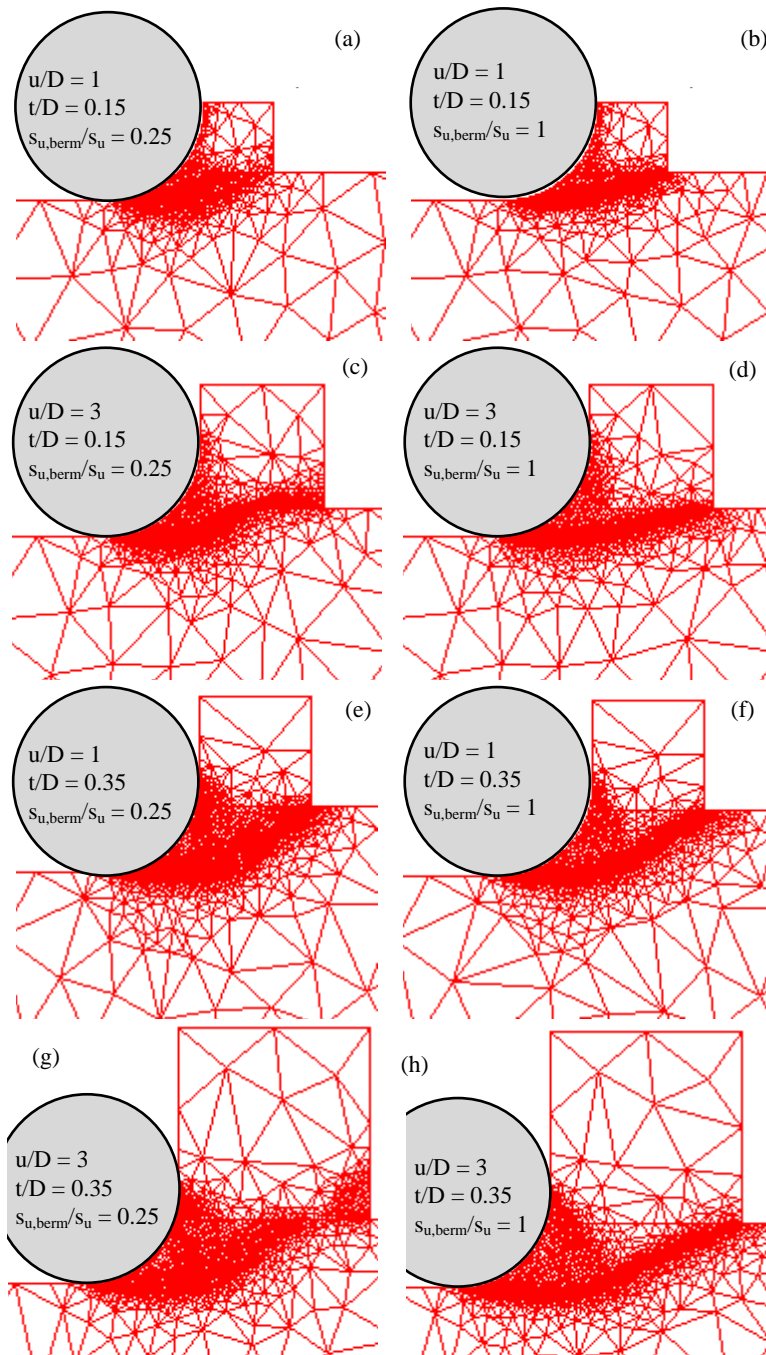
Figure 12. Failure mechanism in a swipe test for (a) – (d) t/D = 0.15 and (e) – (f) t/D = 0.35
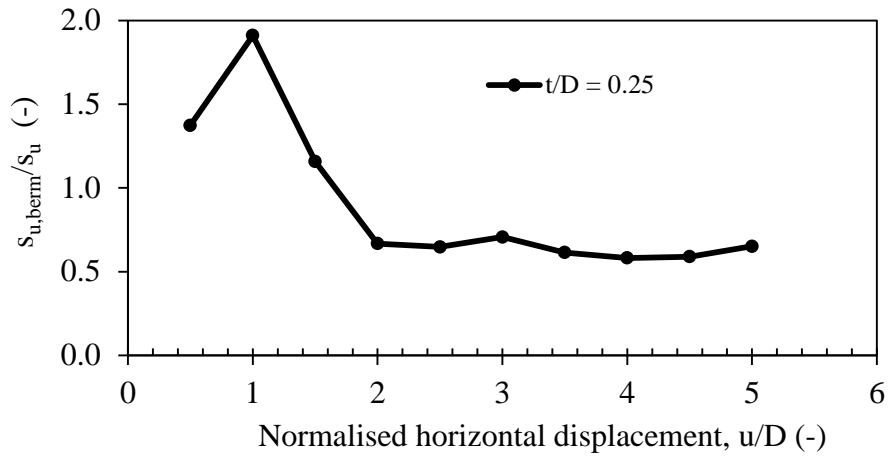
Figure 13. Berm strength at different horizontal positions (t/D = 0.25)
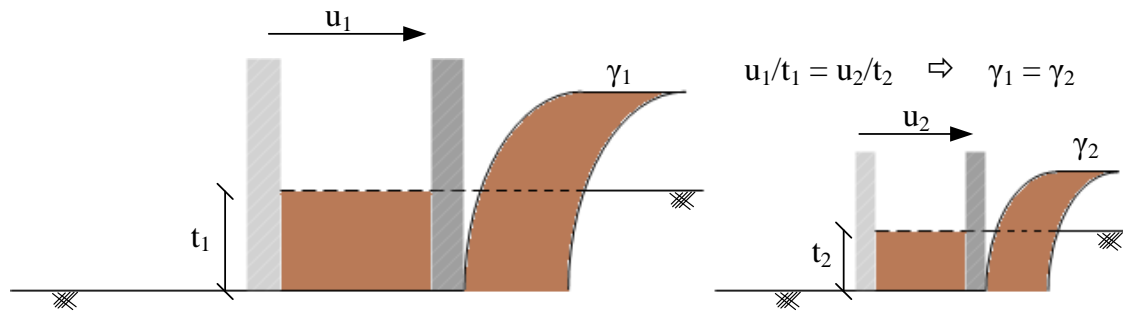
Figure 14. Self-similar berms experience similar level of shear strain
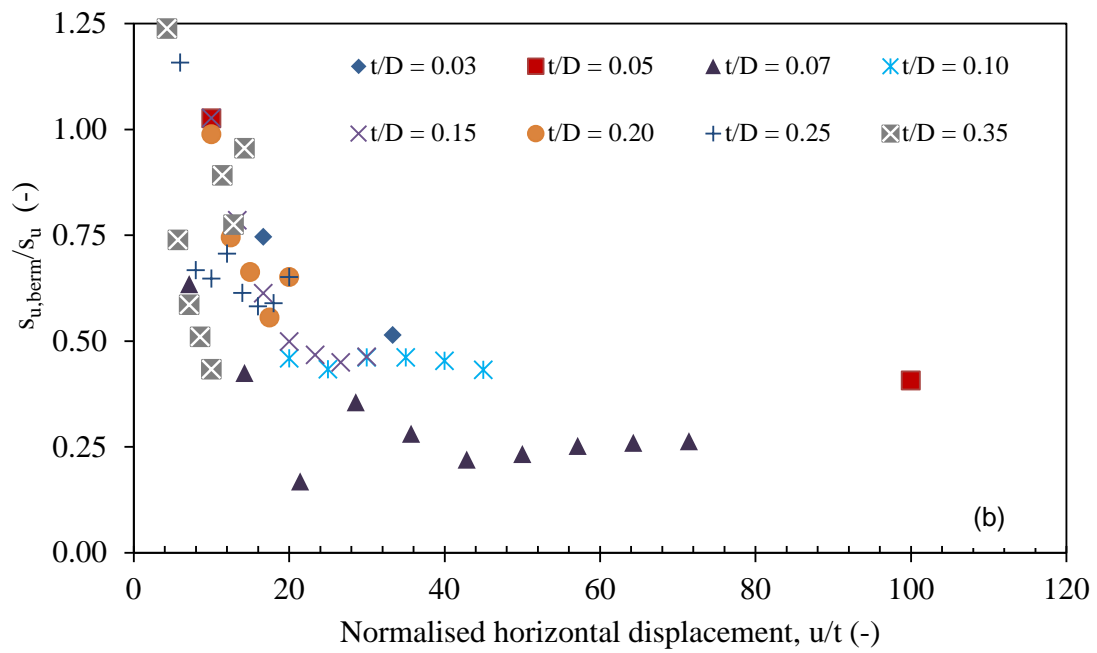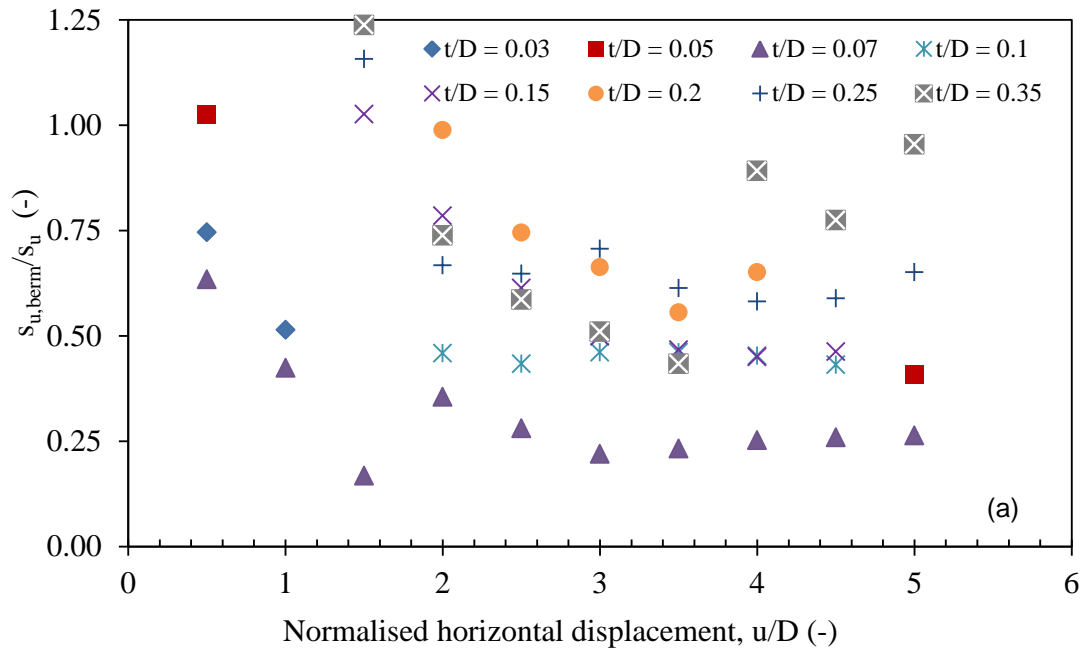
Figure 15. Variations of berm shear strength as a function of travel distance normalised with: (a) pipe diameter; (b) scraping thickness
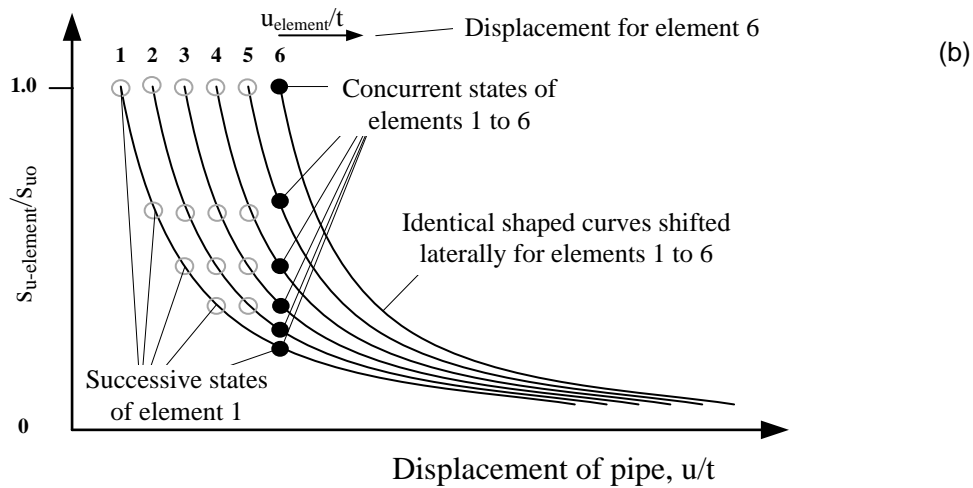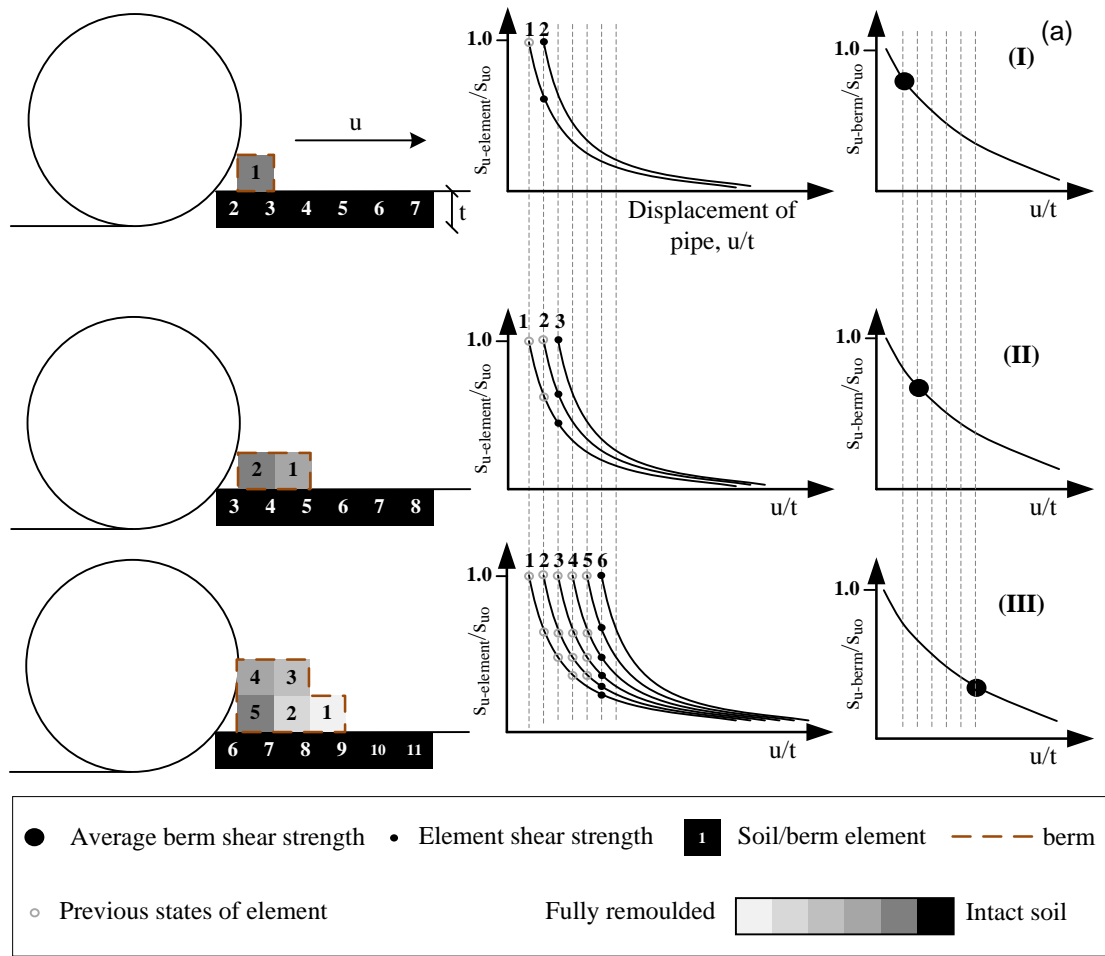
Figure 16. (a) Shear strength of berm and its constituent elements; (b) replot of the middle plot for case III.
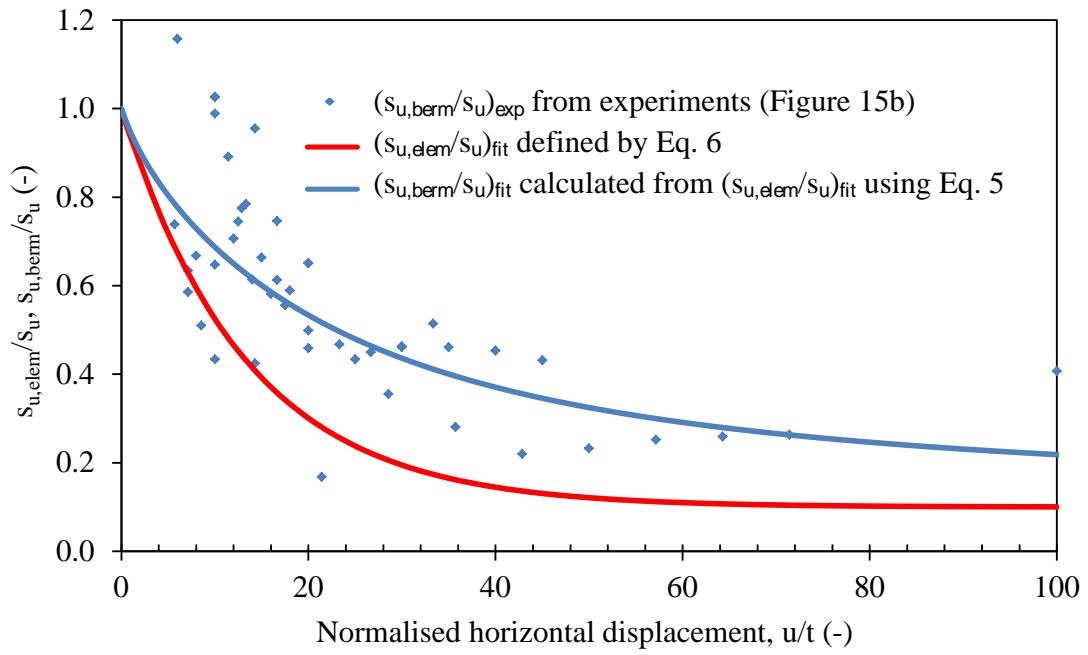
Figure 17. Remoulding of a constant volume of soil with travel distance, $s_{u,elem}$; and berm undrained shear strength - repeat of Figure 15b